# Review of integrated magneto-optical isolators with rare-earth iron garnets for polarization diverse and magnet-free isolation in silicon photonics [Invited]

KARTHIK SRINIVASAN<sup>1,2,3</sup> and Bethanie J. H. Stadler<sup>1,4</sup>

**Abstract:** Passive optical isolators are needed in silicon photonics but unavailable due to challenges in rare-earth iron garnet processing and integration. Material challenges include incompatibility with silicon and high annealing temperatures, and design challenges include a need for polarization diversity and a preference for no external magnetic bias. These challenges have restricted optical isolation to discrete modules that require physical pick and place of bulk garnet pieces. This review presents developments in the processing of magneto-optical garnets on Si and the enhancement of their Faraday rotation that enables small footprint isolators on silicon waveguide structures. For example, seedlayers and/or new garnet compositions have enabled monolithic Si integration, and in some cases, hybrid integration of garnet-on-garnet or transfer-printed garnet nanosheets enable reduced on-chip thermal processing. Integrated isolators that utilize non-reciprocal phase shift (NRPS) or non-reciprocal mode conversion (NRMC) have been demonstrated to have isolation ratios up to 30 dB, insertion loss as low as 9 dB, polarization diversity and magnet-free operation in the desired telecommunication wavelengths. The advances in materials, processing techniques, and isolator designs shown here will pave the way for on-chip isolators and novel multi-lane photonic architectures.

© 2022 Optica Publishing Group under the terms of the Optica Open Access Publishing Agreement

#### 1. Introduction

The ability to deliver large volumes of data at high data rates across a network depends on the capacity of physical data channels. Despite advancements in high-speed low-power optical fiber technologies and multiplexing schemes, most short distance data exchange still happens over electrical pathways [1]. Specifically, within a network switching infrastructure, pluggable transceivers are widespread as the optical-electrical interface and data routing is performed through a complementary metal-oxide-semiconductor (CMOS) based application specific integrated circuit (ASIC). The disconnect between the optical input/output and switching circuitry results in a bottleneck at the low-bandwidth electrical pathways, affecting the network speed and capacity. While a photonic interconnect holds promise in improving the bandwidth, network hardware often trades performance for power, and only few chip-scale functions like multiplexing and modulation happen in the photonic layer [1–3]. An end-to-end optical connectivity is impeded by the lack of a deployable solution for a chip-scale photonic platform that can exceed the performance of hybrid opto-electrical infrastructures, while meeting the size, weight, and power (SWaP) budget of the network.

Alternatively, co-packaged optics (CPO) are a combination of integrated silicon photonics and CMOS switching circuits manufactured using standard semiconductor foundry processes

#447398 Journal © 2022 https://doi.org/10.1364/OME.447398

Received 1 Nov 2021; revised 11 Jan 2022; accepted 13 Jan 2022; published 25 Jan 2022

<sup>&</sup>lt;sup>1</sup>Department of Electrical and Computer Engineering, University of Minnesota – Twin Cities, Minneapolis, MN 55455, USA

<sup>&</sup>lt;sup>2</sup>Currently with the Department of Electrical and Computer Engineering, Cornell University, Ithaca, NY 14850, USA

<sup>&</sup>lt;sup>3</sup>srini162@umn.edu

<sup>&</sup>lt;sup>4</sup>stadler@umn.edu

[4,5]. CPO architectures integrate transceivers and switches on single multi-chip modules (MCM), bringing together optical I/O such as lasers, isolators and photodetectors, electro-optical modulators, and CMOS logic. This reduces the length of electrical pathways between the transceiver and the switching ASIC. While transceiver data rates have steadily increased over the current state-of-the-art (400 Gbps), further improvement is possible only through parallelization using multi-lane schemes at higher baud rates [6]. Higher data rates with parallel lanes will also require integration of multiple lasers and optical isolators in a small footprint. This is possible only when isolators are integrated with silicon waveguide structures and are matched to the mode and dimensions of integrated lasers. Although, lasers that can withstand reflections in the absence of an isolator have been demonstrated, an integrated isolator will significantly reduce the noise floor in any chip and pave the way for highly scalable photonic designs on par with very large-scale integration (VLSI) circuits. It is evident that an integrated optical isolator is the 'missing link', and a multi-faceted approach is required in overcoming the challenges to realizing a foundry-compatible material process and isolator design.

The organization of this review is as follows. First, we provide an overview of rare-earth iron garnets with non-reciprocal properties for optical isolation, techniques to improve garnet Faraday rotation, and challenges in integrating garnet with silicon photonics. This is followed by our contributions in the development of a foundry-friendly high-gyrotropy garnet. Then, select examples of monolithically integrated waveguide isolators that use either non-reciprocal phase shift (NRPS) or non-reciprocal mode conversion (NRMC) is shown. Specifically, the principle of quasi-phase matching and 1D polarization-diverse magnet-free waveguide isolators are elucidated. Lastly, we shift the focus to low thermal budget heterogeneous integration using wafer bonding and conclude with a novel material opportunity for transfer printing exfoliated garnet nanosheets in silicon photonics. While a variety of techniques have been used to develop optical isolators, this review will restrict its scope to Si waveguide isolators using magneto-optical rare-earth iron garnets [7–15].

#### 2. Materials for integrated isolators

#### 2.1. Optical Isolation with rare-earth iron garnets

Optical isolators are non-reciprocal passive devices that are placed in front of a laser to prevent reflections from coupling back into the laser cavity [16,17]. Non-reciprocity is exhibited in isolator materials due to a time-reversal asymmetry caused by non-zero off diagonal elements in their dielectric tensors. As shown in Fig. 1, under a magnetic bias field in the direction of propagation, Zeeman splitting results in a refractive index difference for right and left circularly polarized components of linearly polarized light. This produces a difference in the phase velocity for the two circularly polarized components, which manifests as a rotation of the linear polarization state [18,19]. The asymmetry in the off-diagonal terms produces the same magnitude of rotation in both the forward and reverse direction. This is also known as magneto-optical circular birefringence, or Faraday rotation, or magnetic gyrotropy. The length of the magneto-optical media is varied such that the Faraday rotated reflections are orthogonal to the input polarization, and therefore reflections can be blocked using a linear polarizer [20].

Magneto-optical rare-earth iron garnets (REIG) have been the preferred non-reciprocal material for isolators in the telecom wavelengths (1.33  $\mu m$  and 1.55 $\mu m$ ) since the late 1960s [21–24]. Rare-earth iron garnets are complex oxides with stoichiometries of Re<sub>3</sub>Fe<sub>5</sub>O<sub>12</sub> in cubic structures, lattice parameters of 12-13 Å, and three cation sublattices each [25,26]. Different rare-earth (RE) elements from the Lanthanoid series have been demonstrated to form a stable iron garnet phase. In a REIG, the rare-earth cation occupies 8 O<sup>2-</sup>-coordinated dodecahedral site (c), while the iron occupies both 6 O<sup>2-</sup>-coordinated octahedral (a) and 4 O<sup>2-</sup>-coordinated tetrahedral sites (d). Importantly, in a garnet lattice, there are 3 tetrahedral sites for every 2 octahedral sites, resulting in an unequal distribution of Fe<sup>3+</sup> cations between the two sublattices. The

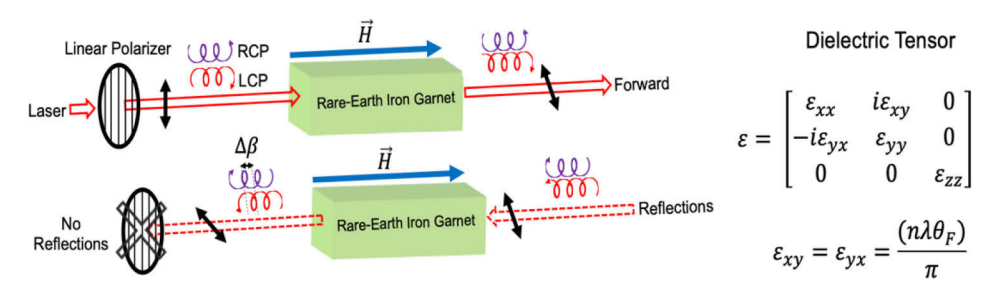


**Fig. 1. Optical Isolation.** (left) Illustration of an optical isolator: The non-reciprocity in the rotation of linear polarization from the magneto-optical media (rare-earth iron garnets) results in reflections that are orthogonal to the input polarization state. (right) Dielectric tensor with non-zero off-diagonal components that are functions of wavelength  $(\lambda)$  and Faraday rotation  $(\theta_F)$ .

cation spins in the dodecahedral and octahedral sites are coupled ferromagnetically but coupled antiferromagnetically to the cation spins in the tetrahedral site. This leads to a ferrimagnetic structure in REIG [22]. The Faraday rotation in a garnet is a function of wavelength and temperature, which is expressed as a sum of products of dipole transition coefficients  $(C(\lambda), A(\lambda))$  and  $D(\lambda)$  and magnetizations for each cation sublattice  $(M_c(T), M_a(T))$  and  $M_d(T)$ ).

$$\theta_F(T, \lambda, H) = \pm C(\lambda)M_c(T) \pm A(\lambda)M_a(T) \mp D(\lambda)M_d(T) \tag{1}$$

The upper signs are for  $T < T_{comp}$  and the lower signs are for  $T > T_{comp}$ , where  $T_{comp}$  is the compensation temperature at which the magnetic sublattices are perfectly antiferromagnetically balanced for a net zero magnetization. The magnetic dipole transition coefficient for  $Fe^{3+}$  in the tetrahedral and octahedral sites are largely non-dispersive in the infrared and only depend on the Landé g-factor. However, parity allowed electric dipole transitions can arise from intraorbit transitions between 3d orbitals in  $Fe^{3+}$  and interorbit transitions between the 4f and 3d orbitals of rare-earth dopants (like  $Ce^{3+}$ ) and  $Fe^{3+}$  [27,28].

Enhancing Faraday rotation in a garnet is critical to obtaining short footprint devices and to transition from bulk pieces of garnet to integrated waveguide devices for optical isolation. From Eq. (1), the Faraday rotation can be enhanced by increasing the magnitude of the electric and magnetic dipole transition coefficients. Yttrium iron garnet (Y<sub>3</sub>Fe<sub>5</sub>O<sub>12</sub>, YIG) benefits only from the electric and magnetic dipole contributions from Fe<sup>3+</sup>, resulting in a Faraday rotation of +200°/cm at 1550 nm [29]. Similarly, for terbium iron garnet (Tb<sub>3</sub>Fe<sub>5</sub>O<sub>12</sub>, TbIG), the contributions of the electric and magnetic dipole transitions from Fe<sup>3+</sup> and Tb<sup>3+</sup> results in a Faraday rotation of +500°/cm [29]. The difference in sign between the electric dipole contribution from tetrahedral (3) and octahedral (2) sites usually results in a positive Faraday rotation for unsubstituted REIGs even in the presence of a non-zero contribution from the RE at the dodecahedral site [30,31]. When REIGs are preferentially substituted with other RE cations such as Ce<sup>3+</sup> or Bi<sup>3+</sup> at the dodecahedral sites, an enhancement in Faraday rotation is observed [32–35]. Here, in addition to the dipole contributions from the host lattice cations, the strong interorbit electric dipole transitions between the 4f states in Ce<sup>3+</sup> and 3d states in octahedral Fe<sup>3+</sup> results in a large negative Faraday rotation. In BiYIG, Bi<sup>3+</sup> substitution enhances the Faraday rotation in the near-infrared by an increased spin-orbit splitting of optical transitions at 2.8 eV and 3.3 eV, attributed to the electron charge transfer transition pairs between the octahedral and tetrahedral Fe<sup>3+</sup> cations [36]. Cations in a garnet lattice have an oxidation state of 3+, and presence of 2 + and 4 + states must cancel each other or can lead to increased optical absorption (from charge transfer process between  $Fe^{2+}$  and  $Fe^{3+}$ ), detrimental to the figure of merit.

Early isolators were made of a bulk assembly of terbium gallium garnet (TGG) or YIG between two permanent magnets and polarizing filters that would be placed in the light path using physical pick and place techniques [37]. While advancements in material growth techniques have resulted in latched garnets that operate without an external bias magnetic field, garnets are still only integrated heterogeneously as discrete optics with ball lenses that route the light to an underlying photonic layer [38–40]. Designing an isolator in the photonic layer would require garnet integration with semiconductor platforms, which has been historically prevented by a mismatch in the coefficient of thermal expansion (CTE) between the two material systems.

#### 2.2. Monolithic integration of rare-earth iron garnets

Monolithic integration of garnets on silicon waveguides is achieved using sputter deposition or pulsed laser deposition (PLD) followed by rapid thermal annealing at 750-950 °C. Sung et al. demonstrated the first successful growth of YIG in the desired phase of Y<sub>3</sub>Fe<sub>5</sub>O<sub>12</sub> on non-garnet substrates (quartz and MgO) using radio-frequency (RF) magnetron sputtering and an annealing temperature of 700-800 °C [41]. On more commonly used planar Si substrates, the interface area between YIG and silicon exacerbated the thermal expansion and caused cracking. Patterning garnets into waveguides reduced the effective area at the interface and resulted in successful growth of high quality YIG on semiconductor platforms. However, substituted garnets (eg: BiYIG and CeYIG), which had the potential for large Faraday rotations, produced secondary phases and had poor crystallinity when grown using a similar process on Si. Bi et al. discovered that a 20 nm seedlayer of YIG promoted desired phase growth of CeYIG and BiYIG on Si substrates with a Faraday rotation of -830°/cm using PLD, which was subsequently improved to -1100°/cm with a 30 nm seedlayer [42,43]. Further, Block et al. showed that a foundry compatible technique like sputtering (Fig. 2(a)) can also be used to grow doped garnets and found that an optimal thickness of 45 nm for the seedlayer (Fig. 2(c)) results in 100% crystallization of CeYIG with a large Faraday rotation of -3700°/cm, Fig. 2(e) [44].

While an undoped YIG seedlayer provides a means to monolithically integrate garnets on semiconductor substrates, it also requires multiple lithography steps for select area deposition and consequently multiple high temperature annealing processes. Previous research from Block et al. and Bi et al. have reported that REIGs require up to 900 °C in an RTA for desired phase crystallization [44,46]. Sun et al. proposed a single step process where CeYIG is deposited first on Si followed by a top seedlayer of YIG (20 nm) (Fig. 2(b)) such that nucleation is initiated at the top layer and acts as a template for the underlying CeYIG as shown in Fig. 2(d) [45]. Here, a Faraday rotation of -1100°/cm is reported for the single-step Si/CeYIG/YIG bilayer crystallized in the desired phase (Fig. 2(f)). Top seed layers of undoped YIG have also been used in obtaining Faraday rotations greater than -2800°/cm in Dy substituted CeYIG (Dy:CeYIG) deposited with a substrate temperature of 400 °C and a post-deposition ex-situ RTA at 850 °C [47]. While cerium substitution has improved Faraday rotation, the absorption tail from a Ce transition at 933 nm (or 1.3 eV) can extend into the infrared near the operating wavelength of most telecommunication isolators at 1330 nm or 1550 nm. Bismuth substituted YIG, which does not have a detrimental absorption peak near IR, is a favorable alternative and in fact, most garnets in bulk isolators are BiYIG [32,48]. Successful monolithic integration of BiYIG on Si has been achieved through sputtering (with bottom YIG seedlayer) and PLD (either top or bottom YIG seedlayer) with Faraday rotations > -1800 °/cm and ex-situ RTA at 800-850 °C [44,48]. A summary of rare-earth iron garnets along with the thickness of seedlayers, Faraday rotation, and impact on thermal budget is given in Table 1.

Although YIG seedlayers are essential in obtaining large Faraday rotations in integrated isolators, they are optically active with a Faraday rotation contribution > +200 °/cm. The opposite chirality of the gyrotropy is detrimental for garnet claddings as the effective rotation experienced by the evanescent tail of the propagating mode decreases. While top seed layers do

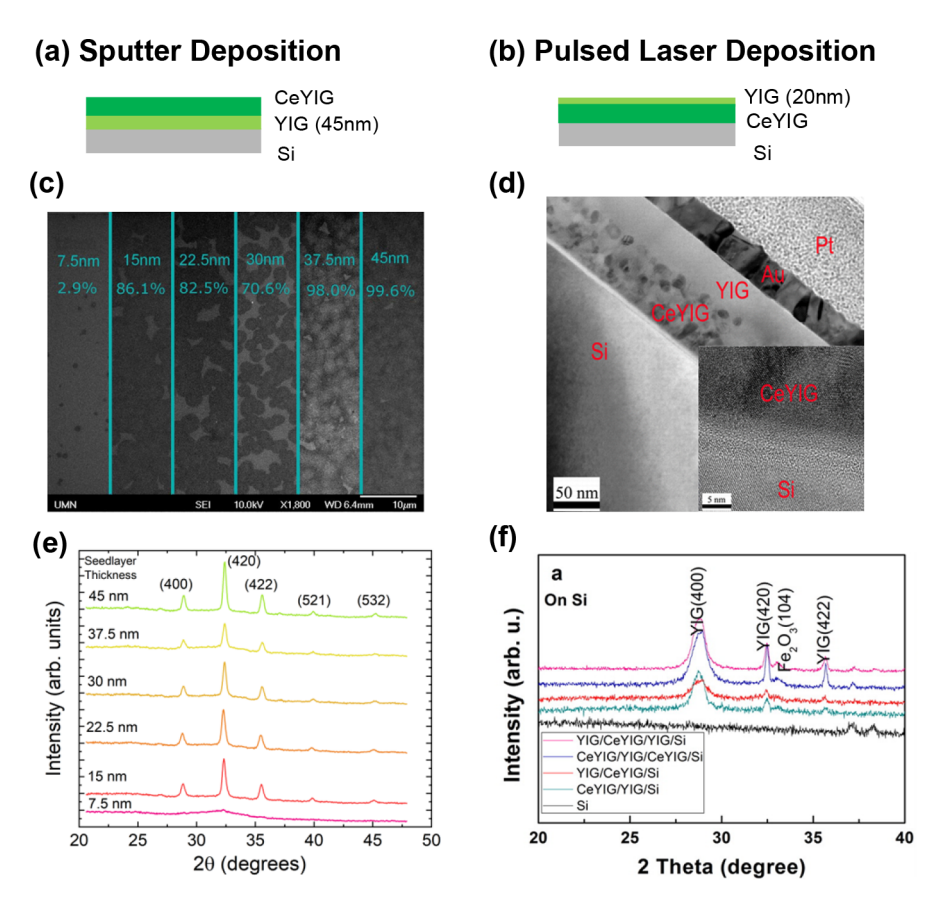


**Fig. 2.** Physical Vapor Deposition (PVD) of substituted rare-earth iron garnets. (a) and (b) Illustration of bottom and top seed layers from RF magnetron sputter deposition and pulsed laser deposition (PLD), respectively. (c) Progression of crystallinity in sputtered CeYIG with different thickness of seedlayers on silicon substrates from scanning electron microscope. (d) Bright-field cross-section transmission electron microscope (TEM) image of PLD YIG/CeYIG/Si and high-resolution TEM image of the interface between CeYIG and Si (inset). (e) and (f) X-ray diffraction spectra of CeYIG/YIG/Si deposited on seedlayers of varying thicknesses and PLD CeYIG with top and bottom seedlayers on Si, respectively. Panels (c) and (d) are reproduced from [44] under the *Creative Commons license*. Panels (d) and (f) are reproduced from [45]. Further permissions related to the material excerpted should be directed to the ACS. https://pubs.acs.org/doi/full/10.1021/acsphotonics.5b00026.

not reduce Faraday rotation, most waveguide isolators in the literature use a bottom seed layer. This leads to a trilateral problem where waveguide isolators with high-gyrotropy garnets need a thin seedlayer, seedlayers introduce multiple lithographic/annealing steps, and RTA temperatures beyond 800 °C further push the limits of available thermal budget in a standard foundry process. Lastly, most monolithic isolators still require an external magnetic bias provided through an on-chip electromagnet or bulk permanent magnets, increasing the complexity of integrating isolators with Si photonics.

## 2.3. Seedlayer-free rare-earth iron garnets

Uninhibited interaction of a propagating mode in a Si core isolator can be obtained through a seedlayer-free garnet cladding. Dulal *et al.* developed the first seedlayer-free terbium iron

Table 1. Summary of select rare-earth iron garnets for monolithic and heterogeneous integration with Si photonics.

Garnet/ Substrate	Deposition/ Growth Process	Seedlayer (Thickness)	Faraday Rotation (°/cm)	Impact on Thermal Budget $({}^{\circ}C)^a$	Reference					
Monolithic Integration										
Ce <sub>1</sub> YIG/Si	PLD	20 nm YIG	-830	850	[43]					
Bi <sub>1.8</sub> YIG/Si	FLD		-838	830	[43]					
Ce <sub>1</sub> YIG/Si	PLD	31 nm YIG	-1100	800	[42]					
Ce <sub>1</sub> YIG/Si	PLD	30 nm YIG (top)	-1100	800	[45]					
Ce <sub>1</sub> YIG/Si	Sputtering	45 nm YIG	-3700	825	[44]					
Bi <sub>1</sub> YIG/Si	Sputtering	35 nm YIG	-1700	825						
Bi <sub>1.5</sub> YIG/Si	PLD	50 nm YIG (top) <sup>b</sup>	-2000	800	[48]					
Ce <sub>1</sub> Dy <sub>2</sub> IG/Si	PLD	42 nm YIG (top)	-2840	850	[47]					
Bi <sub>0.05</sub> TbIG/Si	Sputtering	No seedlayer	-500	900	[29]					
Ce <sub>0.45</sub> TbIG/Si	Sputtering	No seedlayer	-3200	900	[49]					
Ce <sub>0.35</sub> TbIG/Si		No seedlayer	-3550	900						
Ce <sub>0.36</sub> TbIG/Si	PLD	No seedlayer	4500	900	[50]					
Bi <sub>0.03</sub> TbIG/Si	PLD	No seedlayer	6200	900	[50]					
Heterogeneous Integration (wafer bonding/transfer printing)										
Ce <sub>1</sub> YIG/GGG	LPE	No seedlayer	-4500	250	[51,52]					
Ce <sub>0.25</sub> TbIG/Si	Exfoliation	No seedlayer	-2900	None	[53]					

<sup>&</sup>lt;sup>a</sup>Impact on thermal budget is quantified as the maximum temperature the wafer is subjected to in the garnet deposition process.

garnet (TbIG) by identifying a combination of cations that have ionic radii ratios (with respect to O<sup>2-</sup> anion) comparable to the naturally occurring phases of garnet [29]. Here, TbIG was shown to crystallize in the desired phase on silicon and other non-garnet substrates under optimal sputter deposition and annealing conditions. However, TbIG had a small Faraday rotation of +500 °/cm, and with preferential substitution of Ce in the dodecahedral sites, a much larger gyrotropy was achieved in cerium doped terbium iron garnets (or CeTbIG). CeTbIG was sputter deposited through reactive co-sputtering of Fe, Tb and Ce in a magnetron RF setup [49]. The as-deposited amorphous thin films were annealed in an ex-situ RTA at temperatures ranging between 800-950 °C in an oxygen ambient to achieve the desired polycrystalline garnet phase. Upon varying the annealing temperature, desired phase crystallinity was obtained starting at 850 °C and for temperatures > 950 °C, the X-ray diffraction pattern showed signs of secondary non-garnet phases, as seen in Fig. 3(a). Gyrotropy followed the phase purity of the garnet films with a Faraday rotation of -2700 °/cm at 900 °C, which decreased rapidly at higher annealing temperatures. Notably, the Faraday rotation of CeTbIG annealed at 900 °C was greater than twice the gyrotropy experienced by the propagating mode in a CeYIG/YIG cladding on Si waveguide (FR = -1250 °/cm).

As mentioned previously, doping is a standard way to improve the gyrotropic properties of a garnet. Several researchers have demonstrated that Faraday rotation tends to increase with the dopant concentration until it reaches an optimal value beyond which the dopant does not preferentially occupy the dodecahedral sites. In sputtering, the dopant concentration can be

<sup>&</sup>lt;sup>b</sup>YIG is deposited as a top seedlayer.

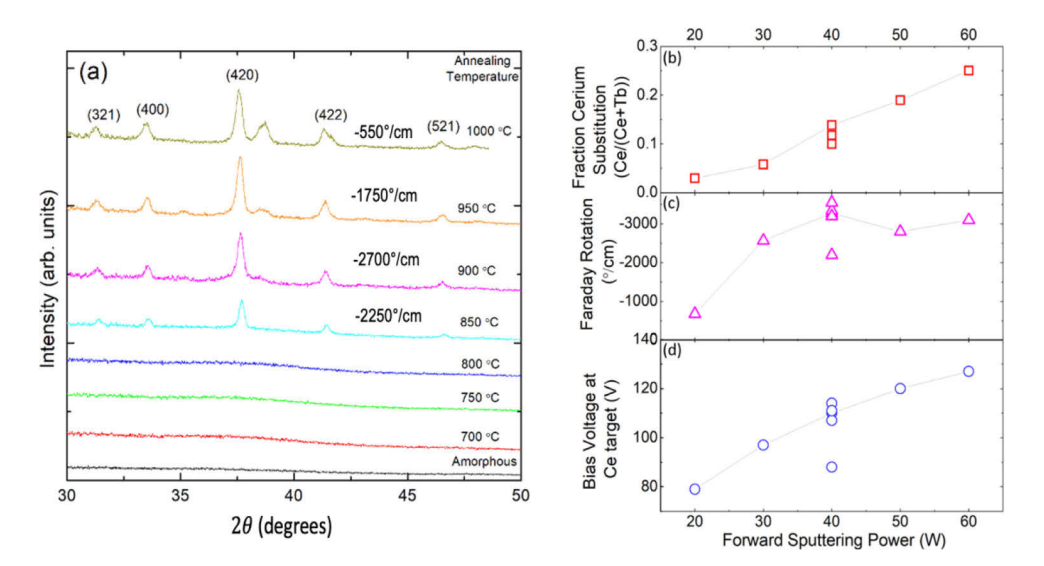


**Fig. 3.** Sputter deposition of cerium doped terbium iron garnet (CeTbIG). (a) X-ray diffractograms of CeTbIG on Si annealed at temperatures from 700°C to 1000 °C with corresponding Faraday rotations for the crystalline thin films. (b) Change in fraction Ce occupying the Tb<sup>3+</sup> lattice sites with increasing forward sputtering power of Ce target. (c) Faraday rotation at 1550 nm in CeTbIG thin films with varying Ce composition. (d) Characteristic dependence of bias voltage at Ce target with forward sputtering power. A low bias voltage resulted in a lower Faraday rotation. Reproduced from [49]. Further permissions related to the material excerpted should be directed to the ACS. https://pubs.acs.org/doi/full/10.1021/acsphotonics.9b00707

varied by adjusting the forward sputtering power of the dopant target. For example, when the sputtering power for a Ce target was varied from 20 to 60 W, the desired phase crystallinity occurred with Ce substituting up to 25% of Tb sites in the lattice, as show in Fig. 3(b) [49].

The ratio of Fe and Ce with respect to the other constituent cations showed that the fraction composition of Fe did not decrease with an increase in fraction substitution of Ce, indicating an absence of anti-site defects in CeTbIG. Furthermore, a large Faraday rotation of  $-3200 \pm 200^{\circ}$ /cm was obtained at an optimal Ce sputtering power of 40 W, Fig. 3(c). However, it was observed that the Faraday rotation of the sputtered film also depended on the bias voltage at the Ce target during sputtering. Bias voltage indicated the surface condition of target (metallic or oxide) when sputtering in an oxidizing environment, where a decrease in bias voltage indicated oxidation of the target. It was shown that repeatable high-gyrotropy in garnets can only be achieved by monitoring the fluctuations in the bias voltage and ensuring the target stayed in the metallic state (or a corresponding stable high bias voltage) throughout the process, as shown in Fig. 3(d). The sputtering processes and garnet stoichiometry reported for high-gyrotropy seedlayer-free CeTbIG have also been successfully adopted for PLD processes to produce large Faraday rotations in Ce- and Bi-TbIG thin films, as shown in Table 1 [50].

#### 3. Integrated isolators for Si photonics

Development of high-gyrotropy garnets, such as CeYIG/YIG, BiYIG/YIG or seedlayer-free CeTbIG or BiTbIG, that could be monolithically integrated paved the way for integrated isolators on semiconductor platforms. Garnet has been incorporated as the cladding or side wall coating on silicon-on-insulator or silicon-nitride  $(Si_3N_4)$ -on-insulator waveguides through physical vapor deposition techniques. Optical isolation has been achieved through device designs that utilized

the non-reciprocal phase shift (NRPS) or non-reciprocal mode conversion (NRMC) depending on the design and direction of external bias magnetic field with respect to the propagating mode [54,55].

#### 3.1. Isolation from non-reciprocal phase shift (NRPS) in interferometers and resonators

In design configurations where the magnetic field is transverse to the direction of light propagation, the guided mode experiences a non-reciprocal phase shift, which can be utilized in an interferometer or ring resonator to achieve unidirectional propagation [43,56,57]. As shown in Fig. 4(a), in an interferometer, this can be achieved by designing the geometric length difference between the two branches of a Mach-Zehnder Interferometer (MZI), such that the reciprocal phase shift is  $\pi/2$ , and the non-reciprocal phase difference is  $-\pi/2$  ( $\pi/2$ ) in the forward (reverse) directions.

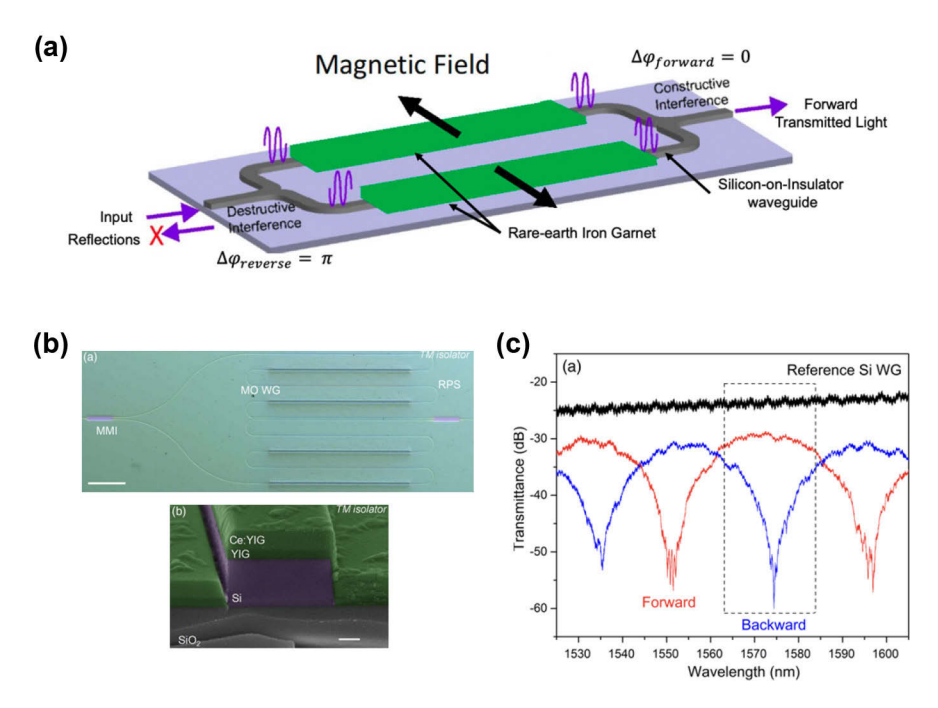


**Fig. 4.** Optical isolation using non-reciprocal phase shift (NRPS). (a) Illustration of Mach-Zehnder Interferometer (MZI) with magneto-optical cladding and bidirectional magnetic bias. (b) Optical micrograph and SEM image of TM-mode isolator with CeYIG/YIG/Si cladding. (c) Forward and backward transmission spectra of the TM-mode isolator from (b). Panels (b) and (c) are reprinted with permission from [58] © The Optical Society.

Some of the early and prominent efforts in monolithic integration of garnets were demonstrated through pulsed laser deposition on NRPS waveguide isolators. Bi *et al.* were the first to demonstrate a monolithically integrated isolator with PLD CeYIG/YIG (seedlayer) on a ring resonator design. [46] This device had an isolation ratio of 20 dB and an unfavorably high insertion loss of 19 dB with a small footprint of 290  $\mu$ m. Further improvements were shown by Zhang *et al.* through a push-pull MZI for both TM and TE modes with top cladding and side wall coating of the garnet, respectively, as shown in Fig. 4(b) [58]. The TM mode isolators had an isolation ratio of 30 dB over a narrow band and an insertion loss of 5-6 dB (Fig. 4(c)), while the TE mode isolators had an isolation ratio of 30 dB and an insertion loss of 9 dB. The footprints of these devices were also under 1 mm², which are some of the smallest monolithic

devices shown in the literature. NRPS designs have also been extended to isolators on  $\mathrm{Si}_3\mathrm{N}_4$  and chalcogenide glass (ChG) waveguides in both interferometer and ring resonator geometries. Yan *et al.* achieved a wideband isolation ratio of 30 dB and an insertion loss of 3 dB over a 16 nm 10 dB bandwidth in an MZI isolator with SiN wavguides and CeYIG/YIG claddings [59]. Narrowband ring resonators with 40 dB isolation were demonstrated with strip-loaded GeSbSe ChG waveguides fabricated on a CeYIG/YIG underlayer, which also eliminated the detrimental effect of positive gyrotropy from YIG seedlayer [60]. Table 2 summarizes isolators with Si waveguide based on the NRPS effect and their performance metrics.

Table 2. Summary of select isolators with Si waveguide and rare-earth iron garnet cladding for integrated Si photonics.

	Isolator Design	Cladding	Mode	Isolation Ratio (dB)	Insertion Loss (dB)	Footprint <sup>a</sup>	Ref.				
	Monolithic Integration - PLD										
NRPS Isolators	Ring Resonator	CeYIG/YIG	TM	19.5	18.8	290 μm	[46]				
	MZI	CeYIG/YIG	TM	30	5-6	0.94 mm x 0.33 mm	[58]				
			TE	30	9	0.87 mm x 0.34 mm					
	Heterogeneous Integration - Direct Bonding										
	MZI	CeYIG	TM	21	8	4 mm x 1 mm	[51]				
S Is	MZI	CeYIG	TM	27	13	1.5 mm x 0.5 mm	[70]				
NRP	Phase Shifter	CeYIG	TM/TE	20	3.2	1.5 mm x 1.5 mm	[71]				
	Ring Resonator	CeYIG	TM	32	10	0.15 mm x 0.07 mm	[72]				
	MZI	CeYIG	TM	29	9	2 mm x 0.5 mm	[73]				
	MZI with Mode Converter	CeYIG	TE	30	18	2-3 mm x 0.5 mm	[74]				
	Heterogeneous Integration - Adhesive Bonding										
	MZI	CeYIG	TM	25	8.1	4 mm x 4 mm	[75]				
	MZI	CeYIG	TE	32	22	6 mm x 0.2 mm	[63]				
	Monolithic Integration - Sputtering										
NRMC Isolators	QPM Faraday Rotator <sup>b</sup>	BiTbIG	TE/TM	30	4.6	4.1 mm x 500 nm	[76]				
		CeYIG/YIG		30	6	5.5 mm x 500 nm	[49]				
		CeTbIG		30	7	7.35 mm x 500 nm					

<sup>&</sup>lt;sup>a</sup>The footprint of isolators with heterogeneously integrated garnet are limited by the size of the wafer bonded garnet die.

TM mode MZI isolators require a top cladding of garnet and magnetization transverse to the direction of light propagation. Early TM mode designs used a bidirectional magnetic field as shown in the schematic of Fig. 4(a) [61,62]. Further improvements used serpentine waveguides in a push-pull configuration (Fig. 4(b)) that allowed the magnetic field to be unidirectional [58,63]. On the other hand, MZI isolators operating in the TE mode required the garnet to be deposited on one of the side walls of the waveguide and magnetized in the out-of-plane direction. Since the NRPS effect (measured in rad/cm) is different for TE and TM modes, longer devices were needed for TE mode isolation compared to TM mode. However, all present lasers for photonic circuits are TE mode, the shorter (and easier to fabricate) TM-mode isolators present other design challenges. These are usually overcome by reciprocal polarization converters or RPC (TE to TM

 $<sup>^</sup>b\mathrm{NRMC}$  QPM waveguide isolators can operate without an active external magnetic bias.

mode and vice versa), which is equivalent to a bulk birefringent plate with an optic axis at  $45^{\circ}$  to the wafer normal. RPCs usually add an additional 100-250  $\mu m$  to the device footprint and require fabrication processes with stringent tolerances for the cross-sectional waveguide profile [64–68].

While isolators in the form of an interferometer or ring resonator have demonstrated desirable isolation characteristics and small footprints, Huang *et al.* have shown that Si cores with > 500 nm are needed for heterogenous III-V laser integration but NRPS effect is possible only when the waveguide height is between 200-250 nm [69]. The mismatch in the Si core thickness between the laser coupler and the isolator will require additional tapers, which are likely to create new sources of reflections into the laser. This unintended consequence of integrating 220 nm core isolators, combined with the fabrication and packaging challenges associated with a seedlayer garnet and incorporation of on-chip electromagnets, has posed severe limitations in the adoption of integrated optical isolators for Si photonics.

## Dimension and Mode Matching with Magnet-Free Non-Reciprocal Mode Conversion (NRMC) Isolators

Non-reciprocal mode conversion design involves a simpler geometry for integrated isolation, just an isotropic waveguide and a magneto-optical cladding to achieve monotonic conversion between the TE and TM modes. NRMC isolators match the dimension and mode of an integrated laser, eliminating the need for tapers before the isolator to provide isolation at the source, as shown in Fig. 5. Moreover, thicker core Si waveguides can be used in NRMC to allow these isolators to be designed on the same photonic layer where the laser is heterogeneously integrated [77]. Mode conversion in an NRMC device is equivalent to a rotation in the linear polarization state of light from  $0^{\circ}$  to  $45^{\circ}$  in the forward direction and  $45^{\circ}$  to  $90^{\circ}$  in the reverse direction. However, due to inherent birefringence in waveguide geometries, coherent conversion often requires periodic loading to overcome the difference in the propagation constants (or modal phase velocity) for the TE/TM modes. See Fig. 6(b) for example of restricted Faraday rotation or mode conversion with modal phase mismatch. Early efforts in alleviating birefringence effects used a magneto-optical waveguide core with a serpentine conductor that alternated the magnetization direction of the garnet to produce a 45° rotation in the forward direction [78]. Wolfe et al. instead alternated the sublattice magnetization through laser annealing such that Ga<sup>3+</sup> changed lattice sites in BiYIG waveguides [79]. However, these devices mostly used a garnet waveguide core or required active elements for periodic loading, neither of which are compatible with the passive design requirements for Si photonics.

#### 3.2.1. Quasi-phase matching

Hutchings *et al.* proposed a quasi-phase matched cladding consisting of alternate segments of magneto-optic and non-magneto-optic material on a Si waveguide to mitigate the modal birefringence (Fig. 6(a)) [64]. The QPM cladding is periodically modulated such that the positive half of the mode beat cycle coincides with the magneto-optical segment ( $L_G$ ) and the negative half of the beat cycle coincides with the nonchiral segment ( $L_N$ ) [80]. Figure 6(b) shows that accumulation of Faraday rotation is restricted to a few degrees without QPM due to birefringence, but with QPM, the accumulated rotation remains constant during each of the negative half-cycles. In such a design, the total accumulated Faraday rotation depends on the number of QPM segments (n) and the gyrotropy of the garnet in each magneto-optic segment. Device footprint ( $n*(L_G + L_N)$ ) can be reduced by using high gyrotropy garnets that reduce the number of QPM segments needed to achieve the required Faraday rotation [81].

The evolution of the modal polarization state in an NRMC waveguide can be visualized using a Poincaré sphere to plot the Stokes parameters, as seen in Fig. 6(c). The polarization state is represented using the Stokes parameters  $(S_0, S_1, S_2 \text{ and } S_3)$ , where  $S_0$  is the total intensity of the propagating beam,  $S_1$  is the preponderance of horizontal over vertical polarization,  $S_2$  is

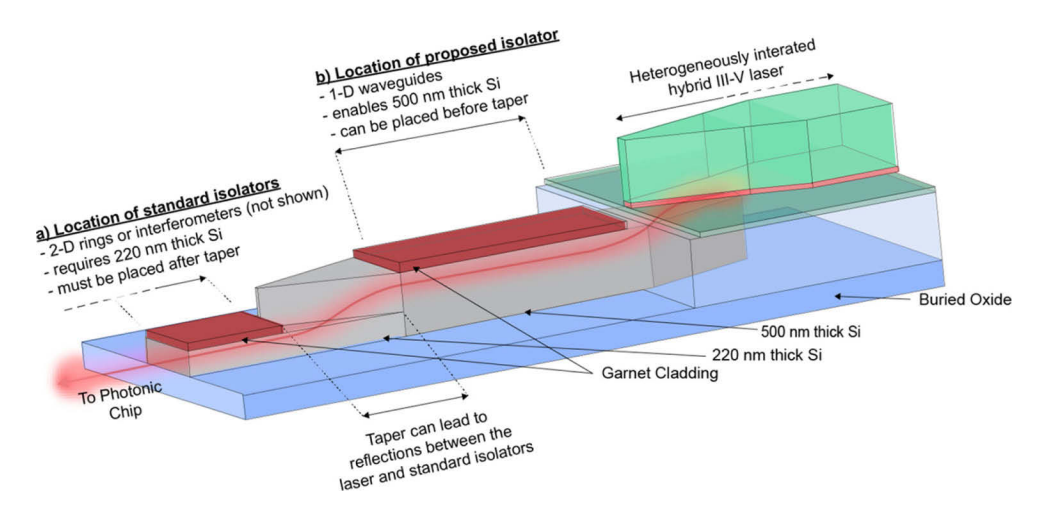


**Fig. 5.** Benefits of isolators that match the mode and dimension of integrated lasers. a) Isolators based on MZI and ring resonators require 220 nm thick Si and must be placed after tapers with requirements for ancillary polarization converters. b) Isolators based on NRMC can use 500 nm thick Si, operate in the TE-mode, and can be designed on the same photonic layer as heterogeneously integrated lasers. Reproduced from [49]. Further permissions related to the material excerpted should be directed to the ACS. https://pubs.acs.org/doi/full/10.1021/acsphotonics.9b00707

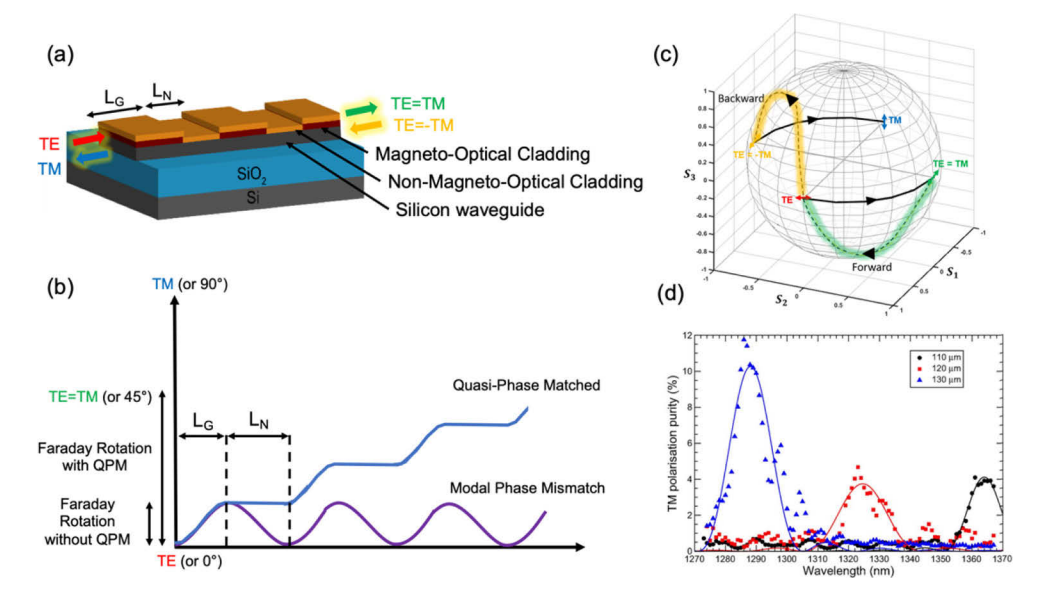


**Fig. 6.** Non-reciprocal mode conversion (NRMC). (a) Quasi-phase matched (QPM) cladding on Si waveguide is used to overcome modal birefringence. (b) Comparison of Faraday rotation or mode conversion (TE to TM) in a rectangular Si waveguide without QPM cladding and with QPM cladding. The MO and non-MO regions are designed to overlap the positive and negative half-cycles of mode. (c) Illustration of polarization state evolution with Stokes parameters on a Poincaré sphere for an NRMC waveguide isolator. (d) TE to TM mode conversion efficiency in early QPM designs on III-V waveguides. © 2013 IEEE. Reprinted, with permission, from [80]

Review

# Optical Materials EXPRESS

the preponderance of  $+45^{\circ}$  over  $-45^{\circ}$  polarization and  $S_3$  is the preponderance of right over left circular polarization states. In the forward direction in an NRMC isolator, half the power from the TE-mode input (at S = (1, 0, 0)) is converted to the TM-mode, resulting in a TE = TM mode (at S = (0, 1, 0)), represented by the solid line along the equator in Fig. 6(c). The photonic chip operates with the TE mode so the TE = TM mode (or 45° linearly polarized light) is rotated through a half-reciprocal polarization converter (H-RPC) (dashed green line in Fig. 6(c)), which is easier to realize than a full reciprocal mode converter that other isolators might use [64]. In the reverse direction, TE-mode reflections go through the H-RPC (dashed yellow line in Fig. 6(c)) where the power is split into TE=-TM (at S = (0, -1, 0)), which is then Faraday rotated to a TM-mode (at S = (-1, 0, 0)) before reaching the laser. This satisfies the orthogonality requirement (or  $\pi$  radians of Stokes vector angle) between the forward and reverse propagating modes for isolation. Although a polarizing filter is used between isolators and lasers in discrete optics, the polarization selectivity of gain media and Bragg mirrors in integrated lasers themselves prevents the TM mode reflections from coupling back into the cavity. Hutchings et al. showed that early designs of a QPM mode converter on III-V waveguides had a TE to TM mode conversion efficiency of 12% as shown in Fig. 6(d) [80].

#### 3.2.2. One-dimensional 'magnet-free' silicon-on-insulator waveguide isolators

The NRMC waveguide isolators have been fabricated using e-beam lithography and garnet liftoff to form the periodic segments that match positive half cycles, followed by deposition of non-magneto-optic  $Si_xN_y$  that match the negative half cycles required for a QPM cladding, as shown in Fig. 7(a). Although prototype devices used e-beam lithography, the dimensions of the waveguide (W x H:  $900 \times 340$ -500 nm) and cladding (21  $\mu$ m QPM segments) are within the fabrication limits of conventional photolithography. Isolation ratios were measured from the angle between the Stokes vector for the forward and reverse propagating modes. Theoretically, the isolation ratio should peak every  $(2n+1)\pi$  radians and is given by  $-10\log(\cos\frac{\theta}{2})^2$ , where

 $\theta = \frac{\overrightarrow{S_f \cdot S_b}}{|S_f| \cdot |S_b|}$  and  $\overrightarrow{S_f}$ ,  $\overrightarrow{S_b}$  are the Stokes vectors for the forward/reverse directions. Figure 7(b) shows the mode conversion peak in terms of the Stokes vector angle and corresponding isolation ratio for a thinner core (340 nm Si) waveguide isolator with seedlayer-free BiTbIG (80 nm) cladding (inset Fig. 7(b)) [76]. The maximum Stokes vector angle for a 3.4 mm long device was  $0.83\pi$  which corresponded to an isolation ratio of -11 dB, and ideal isolation ratio of > 30 dB (or Stokes vector angle of  $\pi$ ) could be achieved by increasing the waveguide length to 4.1 mm. Here, thinner core Si waveguides enhanced the modal interaction with the claddings, resulting in shorter device footprints.

The summary of isolation ratio and optimal length for NRMC isolators on the 500 nm waveguide core with different garnet claddings in Fig. 7(c) shows that seedlayer-free CeTbIG with a maximum Stokes vector angle of  $0.83\pi$  can achieve isolation ratios > 30 dB in a footprint 7.35 mm [49]. Other garnets with lower gyrotropy need a longer or thinner waveguide to achieve the same isolation ratio. Though devices with CeYIG/YIG had a Stokes vector angle of  $0.74\pi$  and required only 5.5 mm to achieve the ideal isolation ratio, the need for multiple lithography/annealing steps due to the seedlayer complicates its fabrication. Although NRMC isolators are a few mm long, unlike NRPS devices where isolation ratio (or phase shift) is a linear function of device length, NRMC isolation ratios have a sinc<sup>2</sup> dependence on the Stokes vector angle as shown in Fig. 7(d). This means devices measured to have less than ideal isolation ratios require only a marginal increase in waveguide length to achieve a Stokes vector angle of  $\pi$  and > 30 dB isolation ratios. Therefore, the narrow cross-section widths of 500-900 nm and waveguide lengths of few mm make NRMC waveguide isolators quasi-1D, which results in a much higher device density than ring resonators and MZI isolators, as shown in the summary of NRMC devices in Table 2.

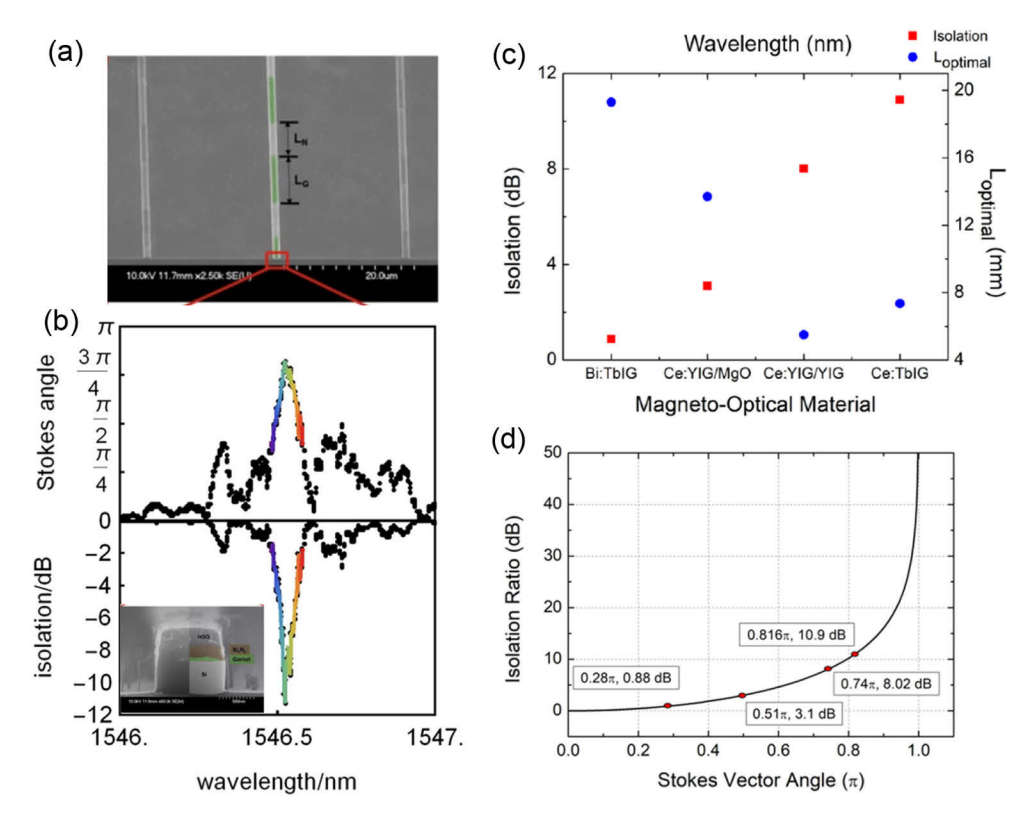


**Fig. 7.** Magnet-free NRMC waveguide isolators with rare-earth iron garnet QPM cladding. (a) SEM image of NRMC waveguide isolators with QPM cladding. The highlighted regions show the periodicity of the magneto-optical cladding [76]. (b) Stokes vector angle and isolation ratio of a 3.4 mm NRMC waveguide isolator with 340 nm thick Si core and BiTbIG cladding (inset). A device length of 4.1 mm would provide > 30 dB isolation. Reproduced from [76] under the *Creative Commons license*. (c) Comparison of measured isolation ratio and optimal waveguide length for > 30 dB isolation in 500 nm thick Si core devices with BiTbIG, CeYIG and CeTbIG cladding. (d) Illustration of the sinc<sup>2</sup> dependence of isolation on the Stokes vector angle shows that ideal isolation ratio in NRMC devices requires only a marginal increase in waveguide length. Panels (c) and (d) are reproduced from [49]. Further permissions related to the material excerpted should be directed to the ACS. https://pubs.acs.org/doi/full/10.1021/acsphotonics.9b00707

It is worth mentioning that in addition to benefitting from a seedlayer-free garnet, NRMC isolators also operate in a remnant magnetization state which is why no external magnetic field was used during the optical measurements of isolators in Ref. [49] and [76]. The quasi-1D nature of the device geometry produces a strong shape anisotropy (easy axis for magnetization) along the length of the waveguide, which is also the direction of the magnetic bias required for isolation. Furthermore, magnetic property investigation into CeTbIG has revealed a large remnance (Mr/Ms = 0.65), low saturation magnetization (18 emu/cc) and preferential in-plane magnetic anisotropy originating from the tensile strain at the garnet/silicon interface [82]. The favorable magnetic properties of CeTbIG in combination with the device geometry allow the NRMC devices to operate without an external magnetic bias.

#### 4. Low-thermal budget isolators with heterogeneously integrated garnets

The discussion so far on monolithic integration of garnets has shown that > 30 dB isolation ratio, < 5 dB insertion loss, polarization diversity and magnet-free operation are possible with NRPS and NRMC devices. However, the high annealing temperature required to crystallize garnets exceeds the temperature limits of back-end of the line CMOS process which is around 575 °C [83]. Early efforts from Gage *et al.* identified a reduced thermal budget process where two steps (at 400 °C and 800 °C) were used to obtain phase pure YIG on SiO<sub>2</sub>/Si substrates [84]. Subsequently, another report demonstrated an annealing temperature of 560 °C for BiYIG on GGG, but foundry-compatible BiYIG on Si required a seedlayer and an RTA step at 800 °C [48]. Despite the efforts in minimizing the annealing temperature, garnet integration with silicon still requires > 800 °C, which risks dopant redistribution in CMOS and solder reflow in integrated circuits. This means that monolithic integration of garnet would need to occur near the beginning of any photonic/electronic integrated chip. Heterogeneous integration of garnets on silicon wafers has been proposed as a feasible alternative that avoids subjecting the chip to a high temperature by growing the garnet on a separate handle wafer and transferring to the photonic chip.

## 4.1. Wafer-bonding

Yokoi et al. proposed the first interferometer based isolator with a wafer bonded magneto-optical garnet cladding to a semiconductor waveguide using surface activated O<sub>2</sub> plasma at 220 °C [85,86]. However, it wasn't until 2008 when Shoji et al. demonstrated a Si waveguide interferometer with wafer bonded CeYIG annealed at 250 °C that had an isolation ratio of 21 dB at 1559 nm [51]. Low temperature integration was also possible with adhesive bonding as shown by Ghosh et al. [75]. Here, 120-150 nm thick polymer of benzocyclobutene (BCB) was used as an adhesive between CeYIG/GGG and the Si interferometer, which resulted in an isolation of 25 dB and insertion loss of 14 dB. While wafer bonding reduced the thermal budget of the process, garnets integrated as top cladding on interferometers limited the mode of operation to TM-mode with a need for bidirectional magnetic fields. Polarization diversity could only be achieved with serpentine interferometers with in-built polarization converters between TE and TM modes [63]. Pintus et al. designed a small-footprint MZI (Fig. 8(a)) with two on-chip electromagnets for the bidirectional magnetic field and polarization rotators that resulted in a TE-mode isolation ratio of 30 dB with a combined loss of 16 dB (Fig. 8(b)) [74]. Here, the insertion loss can be further optimized to 6 dB if the individual losses from bonded facets, couplers and rotators are minimized, which is possible by etching the GGG/CeYIG or improving the precision of bonding alignment. Table 2 provides a summary of interferometers and ring resonators with heterogeneously integrated garnet cladding whose thermal budget is < 250 °C.

## 4.2. Mechanical exfoliation of garnet nanosheets

Transfer printing, a low-temperature alternative to monolithic integration, is a type of hybrid integration that has gained traction in the recent years for its ability to work with inorganic compounds and alloys [87,88]. Usually, transfer printing is possible if the material is directly deposited on a carrier platform or transferred to a carrier platform from a handle wafer through mechanical or chemical exfoliation. Several 2D materials (graphene, MoS<sub>2</sub>, WSe<sub>2</sub> etc.), semiconductor thin films from III-nitrides (GaN etc.) and electro-optical materials (LiNbO<sub>3</sub>) have been successfully exfoliated either through mechanical exfoliation (eg: the Scotch tape method) or a novel process called remote epitaxy [89–93]. In remote epitaxy, a thin layer of graphene is introduced to a substrate (itself via transfer printing) before thin film growth, which allows for sufficient electrostatic interaction for epitaxial film growth yet also allows exfoliation from the substrate. It was only recently, Kum *et al.* shown that epitaxial YIG thin films could

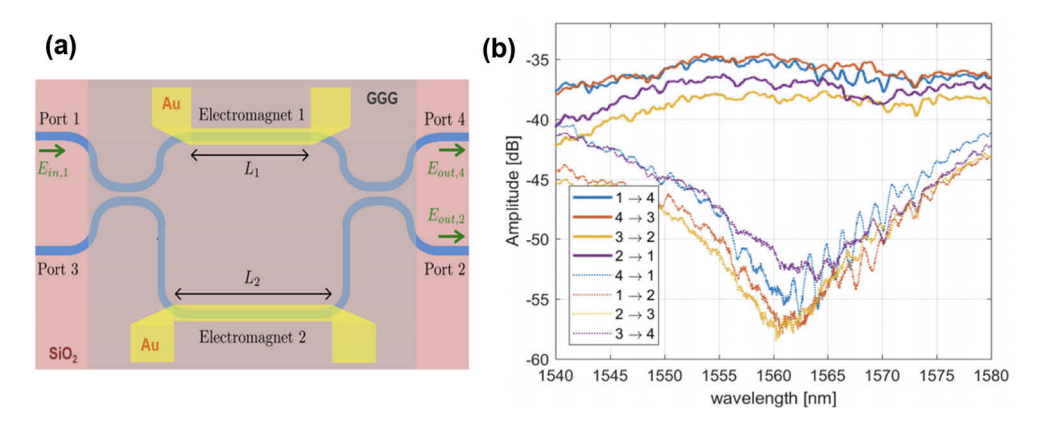


**Fig. 8.** Optical isolators with wafer bonded garnet and on-chip electromagnets. (a) Top view illustration of an MZI isolator/circulator with electromagnet microstrips on the interferometer branches. (b) Transmission spectra of the MZI device in a circulator configuration with isolation of 30 dB between two adjacent ports. © 2019 IEEE. Reprinted, with permission, from [74].

also be exfoliated through remote epitaxy from GGG substrates [94]. However, remote epitaxy of substituted garnets that have high gyrotropy has yet to be demonstrated.

On the other hand, we have shown that large area nanosheets of CeTbIG can be exfoliated from silicon substrates through a diffusion driven creep process without additional interlayers [53]. Creep is a diffusion assisted deformation in crystalline and amorphous materials that occurs at high temperature and low stress [95,96]. Typically, a region under tension (eg: the interface between a film and substrate) has a lower activation energy for vacancy formation than a region under compression. The difference in the vacancy leads to a concentration gradient and therefore to a diffusion of vacancies away from the interface and atoms towards the substrate, as illustrated in Fig. 9(a). Recently, a two-step rapid annealing process that has a short duration spike at 950 °C and a soak at 900 °C was used to introduce a controlled creep of vacancies in CeTbIG/Si, which follow the Nabarro-Herring model of lattice diffusion [97,98]. Through this mechanism, the accumulated vacancies create an exfoliation gap at a distance corresponding to the diffusion length of the cations in garnet. Figure 9(b) shows the optical microscope images of the exfoliated nanosheets on an adhesive tape and Fig. 9(c) shows that the annealed garnets were in the desired polycrystalline phase as indicated by the electron backscattered diffraction (EBSD) image. This was the first report of a diffusion-driven exfoliation mechanism in nanoscale thin films from silicon substrate. Optical and magnetic measurements reveal that the exfoliated nanosheets have a large Faraday rotation of -2900°/cm and a low saturation magnetization of 18 emu/cc, comparable to their thin film properties, as shown in Fig. 9(d). The decrease in coercivity in the exfoliated nanosheets is attributed to a lower magneto-elastic anisotropy compared to the thin films on Si. The desirable optical and magnetic properties, along with the ability to transfer print on Si waveguides will provide an alternative to garnet integration on non-reciprocal devices with minimal impact to the process thermal budget.

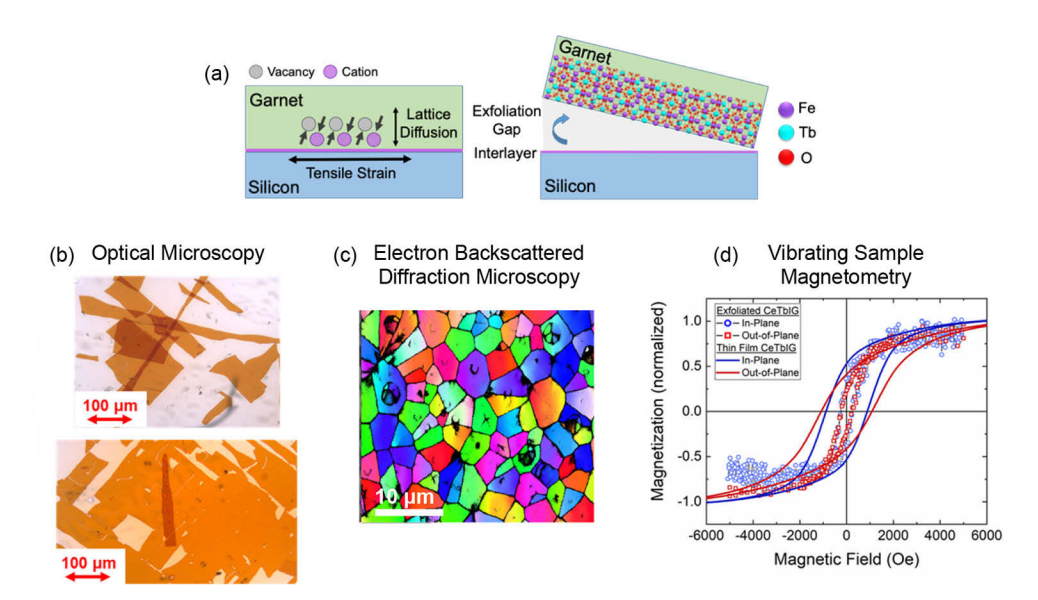


**Fig. 9.** Mechanical exfoliation of rare-earth iron garnet nanosheets. (a) Illustration of the formation of an exfoliation gap and mechanical exfoliation of CeTbIG thin films from diffusion-driven Nabarro-Herring creep mechanism. (b) Optical microscope images of 140 nm exfoliated CeTbIG nanosheets. (c) Electron backscattered diffraction (EBSD) image of a polycrystalline CeTbIG thin film on Si prior to exfoliation. (d) Comparison of magnetic hysteresis between polycrystalline CeTbIG thin films on Si and exfoliated CeTbIG nanosheets. Reprinted (adapted) with permission from [53]. Copyright 2021 American Chemical Society.

#### 5. Summary

This review has presented a comprehensive overview of the developments in magneto-optical rare-earth iron garnets and their integration with a variety of isolator designs for chip-scale isolation in silicon photonics. Effective integration of optical isolators depends on a variety of inter-connected factors such as Faraday rotation, optical losses, thermal budget, modal and dimensional compatibility, footprint, and foundry-compatibility. In the course of developing a suitable magneto-optical material, much of the attention has been on improving the Faraday rotation of rare-earth iron garnets. Doping of garnets with specific rare-earth elements such as Ce and Bi, which enhance the electric and magnetic dipole coefficients at the IR wavelength range, has been established as a reliable technique in achieving large Faraday rotations. Despite having Faraday rotations > -3500°/cm, Ce and Bi substituted yttrium iron garnets have required a seedlayer to crystallize in a useful phase on silicon, which have introduced multiple lithographic steps or high annealing temperatures or both. Seedlayer free garnets based on sputtered terbium iron garnet system have overcome the processing limitations and have shown that consistently large Faraday rotations > -3200°/cm are possible in CeTbIG with precise control of stoichiometry, annealing temperature, and bias voltage at the dopant target. Integrated isolators have been designed using the non-reciprocal phase shift in interferometers and ring resonators or the nonreciprocal mode conversion in waveguide Faraday rotators. NRPS isolators with monolithically integrated garnet have had isolation ratios > 30 dB and insertion losses between 6-9 dB, while achieving polarization diversity and very small footprints. On the other hand, NRMC isolators have used quasi-phase matched cladding to overcome modal birefringence in waveguide structures, and have demonstrated the ability to achieve >30 dB isolation in magnet-free 1D footprints of 4-7 mm. However, the annealing temperatures for monolithic integration in the range of

800-900°C is unsuitable for back-end processing in a photonic foundry line. Heterogeneous integration of garnets through wafer bonding could be achieved at temperatures < 250°C, and these isolators have had isolation ratios >30 dB with integrated electromagnets and polarization diversity through mode converters. The review is concluded with a demonstration of mechanical exfoliation of garnet nanosheets, which provides a glimpse into an emerging possibility of transfer printing garnets onto silicon waveguides while retaining the technological advantages of garnets with no impact to the thermal budget in integrating an optical isolator.

**Acknowledgements.** The authors would like to acknowledge the contributions of Dr. David C. Hutchings. Dr. Cui Zhang, Dr. Sang-Yeob Sung, Dr. Andrew D. Block, Dr. Prabesh Dulal, and Dr. Thomas E. Gage to the research presented in this review. Parts of this work were carried out in the Characterization Facility and the Minnesota Nano Center, which receives partial support from the NSF through the MRSEC (Award Number DMR-2011401) and the Nanotechnology Coordinated Infrastructure (NNCI) program under Award Number ECCS-2025124.

Author Information: Present Address for Dr. Karthik Srinivasan is Cornell University, 302 Phillips Hall, 116 Hoy Road, Ithaca, NY 14850. Email: ks934@cornell.edu

**Disclosures.** The authors declare no conflicts of interest.

**Data Availability.** No data were generated or analyzed in the presented research.

#### References

- D. Dai, J. Wang, and Y. Shi, "Silicon mode (de)multiplexer enabling high capacity photonic networks-on-chip with a single-wavelength-carrier light," Opt. Lett. 38(9), 1422 (2013).
- A. Y. Piggott, J. Lu, K. G. Lagoudakis, J. Petykiewicz, T. M. Babinec, and J. Vučković, "Inverse design and demonstration of a compact and broadband on-chip wavelength demultiplexer," Nat. Photon. 9(6), 374–377 (2015).
- 3. X. Xiao, M. Li, L. Wang, D. Chen, Q. Yang, and S. Yu, "High speed silicon photonic modulators," in 2017 Optical Fiber Communications Conference and Exhibition (OFC) (2017), pp. 1–3.
- R. Stone, R. Chen, J. Rahn, S. Venkataraman, X. Wang, K. Schmidtke, and J. Stewart, "Co-packaged Optics for Data Center Switching," in 2020 European Conference on Optical Communications, ECOC 2020 (Institute of Electrical and Electronics Engineers Inc., 2020).
- C. Minkenberg, R. Krishnaswamy, A. Zilkie, and D. Nelson, "Co-packaged datacenter optics: Opportunities and challenges," IET Optoelectron. 15(2), 77–91 (2021).
- M. Erett, D. Carey, R. Casey, J. Hudner, K. Geary, T. Lee, M. Raj, H. Zhang, A. Roldan, H. Zhao, P.-C. Chiang, H. Zhao, N. Narang, P. Neto, B. Xu, W. Lin, K. H. Tan, Y. Frans, and K. Chang, "A 2.25pJ/bit Multi-lane Transceiver for Short Reach Intra-package and Inter-package Communication in 16 nm FinFET," in 2019 IEEE Custom Integrated Circuits Conference (CICC) (2019), pp. 1–8.
- Q. Lin, J. Wang, and S. Fan, "Compact dynamic optical isolator based on tandem phase modulators," Opt. Lett. 44(9), 2240 (2019).
- 8. S. Longhi, D. Gatti, and G. D. Valle, "Robust light transport in non-Hermitian photonic lattices," Sci. Rep. 5(1), 13376 (2015).
- Y. Shi, Z. Yu, and S. Fan, "Limitations of nonlinear optical isolators due to dynamic reciprocity," Nature Photon. 9(6), 388–392 (2015).
- K. Abdelsalam, T. Li, J. B. Khurgin, and S. Fathpour, "Linear isolators using wavelength conversion," Optica 7(3), 209 (2020).
- T. Amemiya, H. Shimizu, Y. Nakano, P. N. Hai, M. Yokoyama, and M. Tanaka, "Semiconductor waveguide optical isolator based on nonreciprocal loss induced by ferromagnetic MnAs," Appl. Phys. Lett. 89(2), 021104–2007 (2006).
- 12. S. Hua, J. Wen, X. Jiang, Q. Hua, L. Jiang, and M. Xiao, "Demonstration of a chip-based optical isolator with parametric amplification," Nat. Commun. 7(1), 1–6 (2016).
- R. El-Ganainy, A. Eisfeld, M. Levy, and D. N. Christodoulides, "On-chip non-reciprocal optical devices based on quantum inspired photonic lattices," Appl. Phys. Lett. 103(16), 161105 (2013).
- P. Kumar and M. Levy, "On-chip optical isolation via unidirectional Bloch oscillations in a waveguide array," Opt. Lett. 37(18), 3762–3764 (2012).
- 15. E. A. Kittlaus, P. O. Weigel, and W. M. Jones, "Low-loss nonlinear optical isolators in silicon," Nat. Photon. 14(6), 338–339 (2020).
- D. Jalas, A. Petrov, M. Eich, W. Freude, S. Fan, Z. Yu, R. Baets, M. Popović, A. Melloni, J. D. Joannopoulos, M. Vanwolleghem, C. R. Doerr, and H. Renner, "What is and what is not an optical isolator," Nat. Photon. 7(8), 579–582 (2013).
- 17. F. Auracher and H. H. Witte, "A new design for an integrated optical isolator," Opt. Commun. 13(4), 435-438 (1975).
- 18. J. F. Dillon, "Origin and uses of the faraday rotation in magnetic crystals," J. Appl. Phys. 39(2), 922–929 (1968).
- 19. V. J. Fratello, S. E. G. Slusky, C. D. Brandle, and M. P. Norelli, "Growth-induced anisotropy in bismuth: Rare-earth iron garnets," J. Appl. Phys. 60(7), 2488–2497 (1986).
- R. Wolfe, V. J. Fratello, and M. McGlashan-Powell, "Thin-film garnet materials with zero linear birefringence for magneto-optic waveguide devices (invited)," J. Appl. Phys. 63(8), 3099–3103 (1988).

- W. A. Crossley, R. W. Cooper, J. L. Page, and R. P. Van Stapele, "Faraday rotation in rare-earth iron garnets," Phys. Rev. 181(2), 896–904 (1969).
- 22. G. Winkler, Magnetic Garnets (Vieweg, 1981).
- 23. B. J. H. Stadler and T. Mizumoto, "Integrated magneto-optical materials and isolators: a review," IEEE Photon. J. **6**(1), 1–15 (2014).
- 24. K. Srinivasan and B. J. H. Stadler, "Magneto-optical materials and designs for integrated TE- and TM-mode planar waveguide isolators: a review [Invited]," Opt. Mater. Express 8(11), 3307 (2018).
- 25. S. Geller and M. A. Gilleo, "The crystal structure and ferrimagnetism of yttrium-iron garnet, Y<sub>3</sub>Fe<sub>2</sub>(FeO<sub>4</sub>)<sub>3</sub>," J. Phys. Chem. Solids **3**(1-2), 30–36 (1957).
- Ü. Özgür, Y. Alivov, and H. Morkoç, "Microwave ferrites, part 1: fundamental properties," J Mater Sci: Mater Electron 20(9), 789–834 (2009).
- M. Gomi, H. Furuyama, and M. Abe, "Strong magneto-optical enhancement in highly Ce-substituted iron garnet films prepared by sputtering," J. Appl. Phys. 70(11), 7065–7067 (1991).
- 28. M. Kučera, "Magneto-optics of Ce<sup>3+</sup> doped garnets," J. Magn. Magn. Mater. **101**(1-3), 242–244 (1991).
- P. Dulal, A. D. Block, T. E. Gage, H. A. Haldren, S.-Y. Sung, D. C. Hutchings, and B. J. H. Stadler, "Optimized magneto-optical isolator designs inspired by seedlayer-free terbium iron garnets with opposite chirality," ACS Photonics 3(10), 1818–1825 (2016).
- M. Guillot, H. Le Gall, J. M. Desvignes, and M. Artinian, "Faraday rotation of bismuth substituted terbium iron garnets," IEEE Trans. Magn. 30(6), 4419–4421 (1994).
- 31. M. Guillot, P. Feldmann, H. Le Gall, and D. Minella, "Temperature and high magnetic field dependence of the Faraday rotation in the terbium iron garnet," J. Phys. **40**(9), 883–893 (1979).
- 32. V. J. Fratello, "Innovative improvements in bismuth-doped rare-earth iron garnet faraday rotators," IEEE Trans. Magn. 32(5 PART 1), 4102–4107 (1996).
- 33. C. F. Buhrer, "Enhancement of the faraday rotation of iron garnets by bismuth and rare-earth ions," J. Appl. Phys. 41(3), 1393–1394 (1970).
- H. L. Gall, J. M. Desvignes, and M. Artinian, "Faraday rotation of bismuth substituted terbium iron garnets," IEEE Trans. Magn. 30(6), 4419–4421 (1994).
- 35. H. Takeuchi, "The Faraday effect of bismuth substituted rare-earth iron garnet," Jpn. J. Appl. Phys. **14**(12), 1903–1910 (1975).
- 36. S. Wittekoek, T. J. A. Popma, J. M. Robertson, and P. F. Bongers, "Magneto-optic spectra and the dielectric tensor elements of bismuth-substituted iron garnets at photon energies between 2.2-5.2 eV," Phys. Rev. B **12**(7), 2777–2788 (1975)
- 37. H. Yoshida, K. Tsubakimoto, Y. Fujimoto, K. Mikami, H. Fujita, N. Miyanaga, H. Nozawa, H. Yagi, T. Yanagitani, Y. Nagata, and H. Kinoshita, "Optical properties and Faraday effect of ceramic terbium gallium garnet for a room temperature Faraday rotator," Opt. Express 19(16), 15181 (2011).
- D. Karki, V. Stenger, A. Pollick, and M. Levy, "Thin-film magnetless Faraday rotators for compact heterogeneous integrated optical isolators," J. Appl. Phys. 121(23), 233101 (2017).
- 39. M. P. Mack, A. Ayazi, Y. Chi, A. Dahl, P. D. Dobbelaere, S. Denton, S. Gloeckner, K. Y. Hon, S. Hovey, Y. Liang, G. Masini, A. Mekis, M. Peterson, T. Pinguet, S. Sahni, J. Schramm, M. Sharp, C. Sohn, K. Stechschulte, P. Sun, G. Vastola, L. Verslegers, and R. Zhou, "Luxtera's silicon photonics platform for transceiver manufacturing," in 2014 International Conference on Solid State Devices and Materials (2014).
- 40. P. D. D. Michael Mack, Mark Peterson, Steffen Gloeckner, Adithyaram Narasimha, and Roger Koumans, "Method and system for a light source assembly supporting direct coupling to an integrated circuit," patent US8168939B2 (2008).
- S. Y. Sung, X. Qi, and B. J. H. Stadler, "Integrating yttrium iron garnet onto nongarnet substrates with faster deposition rates and high reliability," Appl. Phys. Lett. 87(12), 1–3 (2005).
- 42. T. Goto, M. C. Onbasli, and C. A. Ross, "Magneto-optical properties of cerium substituted yttrium iron garnet films with reduced thermal budget for monolithic photonic integrated circuits," Opt. Express 20(27), 28507 (2012).
- L. Bi, J. Hu, G. F. Dionne, L. Kimerling, and C. A. Ross, "Monolithic integration of chalcogenide glass/iron garnet waveguides and resonators for on-chip nonreciprocal photonic devices," SPIE 7941, 794105 (2011).
- 44. A. D. Block, P. Dulal, B. J. H. Stadler, and N. C. A. Seaton, "Growth parameters of fully crystallized YIG, Bi:YIG, and Ce:YIG films with high Faraday rotations," IEEE Photon. J. 6(1), 1–8 (2014).
- 45. X. Y. Sun, Q. Du, T. Goto, M. C. Onbasli, D. H. Kim, N. M. Aimon, J. Hu, and C. A. Ross, "Single-step deposition of cerium-substituted yttrium iron garnet for monolithic on-chip optical isolation," ACS Photonics 2(7), 856–863
- 46. L. Bi, J. Hu, P. Jiang, D. H. Kim, G. F. Dionne, L. C. Kimerling, and C. A. Ross, "On-chip optical isolation in monolithically integrated non-reciprocal optical resonators," Nat. Photon. 5(12), 758–762 (2011).
- 47. Y. Zhang, Q. Du, C. Wang, W. Yan, L. Deng, J. Hu, C. A. Ross, and L. Bi, "Dysprosium substituted Ce:YIG thin films with perpendicular magnetic anisotropy for silicon integrated optical isolator applications," APL Mater. 7(8), 081119 (2019).
- 48. T. Fakhrul, S. Tazlaru, L. Beran, Y. Zhang, M. Veis, and C. A. Ross, "Magneto-optical Bi:YIG films with high figure of merit for nonreciprocal photonics," Adv. Opt. Mater. 7(13), 1900056 (2019).

- K. Srinivasan, C. Zhang, P. Dulal, C. Radu, T. E. Gage, D. C. Hutchings, and B. J. H. Stadler, "High-gyrotropy seedlayer-free Ce:TbIG for monolithic laser-matched SOI optical isolators," ACS Photonics 6(10), 2455–2461 (2019).
- T. Fakhrul, S. Tazlaru, B. Khurana, L. Beran, J. Bauer, M. Vančík, A. Marchese, E. Tsotsos, M. Kučera, Y. Zhang, M. Veis, and C. A. Ross, "High figure of merit magneto-optical Ce- and Bi-substituted terbium iron garnet films integrated on Si," Adv. Opt. Mater. 9(16), 2100512 (2021).
- Y. Shoji, T. Mizumoto, H. Yokoi, I.-W. Hsieh, and R. M. Osgood, "Magneto-optical isolator with silicon waveguides fabricated by direct bonding," Appl. Phys. Lett. 92(7), 071117 (2008).
- T. Shintaku, T. Uno, and M. Kobayashi, "Magneto-optic channel waveguides in Ce-substituted yttrium iron garnet," J. Appl. Phys. 74(8), 4877–4881 (1993).
- 53. K. Srinivasan, A. Schwarz, J. C. Myers, N. C. A. Seaton, and B. J. H. Stadler, "Diffusion-driven exfoliation of magneto-optical garnet nanosheets: implications for low thermal budget integration in Si photonics," ACS Appl. Nano Mater. (2021).
- 54. W. Bogaerts, D. Taillaert, B. Luyssaert, P. Dumon, J. V. Campenhout, P. Bienstman, D. V. Thourhout, R. Baets, V. Wiaux, and S. Beckx, "Basic structures for photonic integrated circuits in Silicon-on-insulator," Opt. Express 12(8), 1583 (2004).
- B. J. H. Stadler and D. C. Hutchings, "Sputter-deposited magneto-optical garnet for all-mode (transverse electric/transverse magnetic) Faraday rotators," MRS Bull. 43(6), 430–435 (2018).
- J. Fujita, M. Levy, R. M. O. Jr., L. Wilkens, and H. Dötsch, "Waveguide optical isolator based on Mach–Zehnder interferometer," Appl. Phys. Lett. 76(16), 2158–2160 (2000).
- V. Donzella, A. Sherwali, J. Flueckiger, S. M. Grist, S. T. Fard, and L. Chrostowski, "Design and fabrication of SOI micro-ring resonators based on sub-wavelength grating waveguides," Opt. Express 23(4), 4791 (2015).
- 58. Y. Zhang, Q. Du, C. Wang, T. Fakhrul, S. Liu, L. Deng, D. Huang, P. Pintus, J. Bowers, C. A. Ross, J. Hu, and L. Bi, "Monolithic integration of broadband optical isolators for polarization-diverse silicon photonics," Optica 6(4), 473 (2019).
- 59. W. Yan, W. Yan, Y. Yang, Y. Yang, S. Liu, S. Liu, Y. Zhang, S. Xia, S. Xia, T. Kang, T. Kang, W. Yang, W. Yang, J. Qin, J. Qin, L. Deng, L. Deng, L. Bi, and L. Bi, "Waveguide-integrated high-performance magneto-optical isolators and circulators on silicon nitride platforms," Optica 7(11), 1555–1562 (2020).
- Q. Du, C. Wang, Y. Zhang, Y. Zhang, T. Fakhrul, W. Zhang, C. Gonçalves, C. Blanco, K. Richardson, L. Deng, C. A. Ross, L. Bi, and J. Hu, "Monolithic On-chip Magneto-optical Isolator with 3 dB Insertion Loss and 40 dB Isolation Ratio," ACS Photonics 5(12), 5010–5016 (2018).
- A. Erdmann, M. Shamonin, P. Hertel, and H. Dötsch, "Finite difference analysis of gyrotropic waveguides," Opt. Commun. 102(1-2), 25–30 (1993).
- 62. H. Dötsch, N. Bahlmann, O. Zhuromskyy, M. Hammer, L. Wilkens, R. Gerhardt, P. Hertel, and A. F. Popkov, "Applications of magneto-optical waveguides in integrated optics: review," J. Opt. Soc. Am. B 22(1), 240 (2005).
- 63. S. Ghosh, S. Keyvaninia, Y. Shirato, T. Mizumoto, G. Roelkens, and R. Baets, "Optical isolator for TE polarized light realized by adhesive bonding of Ce:YIG on silicon-on-insulator waveguide circuits," IEEE Photon. J. 5(3), 6601108 (2013).
- D. C. Hutchings and B. M. Holmes, "A waveguide polarization toolset design based on mode beating," IEEE Photon. J. 3(3), 450–461 (2011).
- 65. B. M. Holmes and D. C. Hutchings, "Realization of novel low-loss monolithically integrated passive waveguide mode converters," IEEE Photon. Tech. Lett. **18**(1), 43–45 (2006).
- 66. M. R. Watts and H. A. Haus, "Integrated mode-evolution-based polarization rotators," Opt. Lett. **30**(2), 138–140 (2005)
- 67. K. Nakayama, Y. Shoji, and T. Mizumoto, "Single trench SiON waveguide TE-TM mode converter," IEEE Photonics Technol. Lett. 24(15), 1310–1312 (2012).
- J. Zhang, T.-Y. Liow, M. Yu, G.-Q. Lo, and D.-L. Kwong, "Silicon waveguide based TE mode converter," Opt. Express 18(24), 25264–25270 (2010).
- 69. D. Huang, P. Pintus, and J. E. Bowers, "Towards heterogeneous integration of optical isolators and circulators with lasers on silicon [Invited]," Opt. Mater. Express 8(9), 2471 (2018).
- 70. Y. Shoji, Y. Shirato, and T. Mizumoto, "Silicon Mach Zehnder interferometer optical isolator having 8 nm bandwidth for over 20 dB isolation," Jap. J. Appl. Phys. **53**(2), 022202 (2014).
- 71. R. Yamaguchi, Y. Shoji, and T. Mizumoto, "Low-loss waveguide optical isolator with tapered mode converter and magneto-optical phase shifter for TE mode input," Opt. Express 26(16), 21271–21278 (2018).
- 72. D. Huang, P. Pintus, C. Zhang, Y. Shoji, T. Mizumoto, and J. E. Bowers, "Electrically driven and thermally tunable integrated optical isolators for silicon photonics," IEEE J. Sel. Top. Quantum Electron. 22(6), 271–278 (2016).
- D. Huang, P. Pintus, Y. Shoji, P. Morton, T. Mizumoto, and J. E. Bowers, "Integrated broadband Ce:YIG/Si Mach-Zehnder optical isolators with over 100 nm tuning range," Opt. Lett. 42(23), 4901–4904 (2017).
- 74. P. Pintus, D. Huang, P. A. Morton, Y. Shoji, T. Mizumoto, and J. E. Bowers, "Broadband TE optical isolators and circulators in silicon photonics through Ce:YIG Bonding," J. Lightwave Technol. 37(5), 1463–1473 (2019).
- S. Ghosh, S. Keyvavinia, W. Van Roy, T. Mizumoto, G. Roelkens, and R. Baets, "Ce:YIG/Silicon-on-Insulator waveguide optical isolator realized by adhesive bonding," Opt. Express 20(2), 1839 (2012).
- C. Zhang, P. Dulal, B. J. H. Stadler, and D. C. Hutchings, "Monolithically-integrated TE-mode 1d silicon-on-insulator isolators using seedlayer-free garnet," Sci. Rep. 7(1), 1–8 (2017).

- 77. S. Keyvaninia, G. Roelkens, D. Van Thourhout, C. Jany, M. Lamponi, A. Le Liepvre, F. Lelarge, D. Make, G.-H. Duan, D. Bordel, and J.-M. Fedeli, "Demonstration of a heterogeneously integrated III-V/SOI single wavelength tunable laser," Opt. Express 21(3), 3784 (2013).
- P. K. Tien, R. J. Martin, S. L. Blank, S. H. Wemple, and L. J. Varnerin, "Optical waveguides of single-crystal garnet films," Appl. Phys. Lett. 21(5), 207–209 (1972).
- R. Wolfe, J. Hegarty, J. F. Dillon, L. C. Luther, G. K. Celler, L. E. Trimble, and C. S. Dorsey, "Thin-film waveguide magneto-optic isolator," Appl. Phys. Lett. 46(9), 817–819 (1985).
- D. C. Hutchings, B. M. Holmes, C. Zhang, P. Dulal, A. D. Block, S.-Y. Sung, N. C. A. Seaton, and B. J. H. Stadler, "Quasi-phase-matched Faraday rotation in semiconductor waveguides with a magnetooptic cladding for monolithically integrated optical isolators," IEEE Photon. J. 5(6), 6602512 (2013).
- 81. D. C. Hutchings, C. Zhang, B. M. Holmes, P. Dulal, A. D. Block, and B. J. H. Stadler, "Faraday polarisation mode conversion in semiconductor waveguides incorporating periodic garnet claddings," in *Integrated Optics: Devices, Materials, and Technologies XX*, J.-E. Broquin and G. Nunzi Conti, eds. (International Society for Optics and Photonics, 2016), 9750, p. 97500 V.
- K. Srinivasan, C. Radu, D. Bilardello, P. Solheid, and B. J. H. Stadler, "Interfacial and bulk magnetic properties of stoichiometric cerium doped terbium iron garnet polycrystalline thin films," Adv. Funct. Mater. 30(15), 2000409 (2020).
- 83. R. D. Jeffery, R. Sharda, R. C. Woodward, L. Faraone, and M. Martyniuk, "Crystallization of bismuth iron garnet thin films using capacitively coupled oxygen plasmas," J. Appl. Phys. 127(4), 043302 (2020).
- 84. T. E. Gage, P. Dulal, P. A. Solheid, D. J. Flannigan, and B. J. H. Stadler, "Si-integrated ultrathin films of phase-pure Y<sub>3</sub>Fe<sub>5</sub>O<sub>12</sub> (YIG) via novel two-step rapid thermal anneal," Mater. Res. Lett. **5**(6), 379–385 (2017).
- H. Yokoi, T. Mizumoto, N. Shinjo, N. Futakuchi, and Y. Nakano, "Demonstration of an optical isolator with a semiconductor guiding layer that was obtained by use of a nonreciprocal phase shift," Appl. Opt. 39(33), 6158–6164 (2000).
- H. Yokoi, T. Mizumoto, M. Shimizu, T. W. N. Futakuchi, N. Kaida, and Y. Nakano, "Analysis of GaInAsP surfaces by contact-angle measurement for wafer direct bonding with garnet crystals," Jpn. J. Appl. Phys. 38(Part 1, No. 8), 4780–4783 (1999).
- 87. Y. Huang, Y. H. Pan, R. Yang, L. H. Bao, L. Meng, H. L. Luo, Y. Q. Cai, G. D. Liu, W. J. Zhao, Z. Zhou, L. M. Wu, Z. L. Zhu, M. Huang, L. W. Liu, L. Liu, P. Cheng, K. H. Wu, S. B. Tian, C. Z. Gu, Y. G. Shi, Y. F. Guo, Z. G. Cheng, J. P. Hu, L. Zhao, G. H. Yang, E. Sutter, P. Sutter, Y. L. Wang, W. Ji, X. J. Zhou, and H. J. Gao, "Universal mechanical exfoliation of large-area 2D crystals," Nat. Commun. 11(1), 1–9 (2020).
- 88. T. Lan, B. Ding, and B. Liu, "Magneto-optic effect of two-dimensional materials and related applications," Nano Select 1(3), 298–310 (2020).
- 89. H. Li, J. Wu, Z. Yin, and H. Zhang, "Preparation and applications of mechanically exfoliated single-layer and multilayer MoS<sub>2</sub> and WSe<sub>2</sub> nanosheets," Acc. Chem. Res. **47**(4), 1067–1075 (2014).
- M. Onodera, S. Masubuchi, R. Moriya, and T. MacHida, "Assembly of van Der Waals heterostructures: exfoliation, searching, and stacking of 2D Materials," Jap. J. Appl. Phys. 59, 1 (2020).
- 91. J. Jiang, X. Sun, X. Chen, B. Wang, Z. Chen, Y. Hu, Y. Guo, L. Zhang, Y. Ma, L. Gao, F. Zheng, L. Jin, M. Chen, Z. Ma, Y. Zhou, N. P. Padture, K. Beach, H. Terrones, Y. Shi, D. Gall, T.-M. Lu, E. Wertz, J. Feng, and J. Shi, "Carrier lifetime enhancement in halide perovskite via remote epitaxy," Nat. Commun. 10(1), 4145 (2019).
- 92. Y. Kim, S. S. Cruz, K. Lee, B. O. Alawode, C. Choi, Y. Song, J. M. Johnson, C. Heidelberger, W. Kong, S. Choi, K. Qiao, I. Almansouri, E. A. Fitzgerald, J. Kong, A. M. Kolpak, J. Hwang, and J. Kim, "Remote epitaxy through graphene enables two-dimensional material-based layer transfer," Nature 544(7650), 340–343 (2017).
- 93. J. Kim, C. Bayram, H. Park, C. W. Cheng, C. Dimitrakopoulos, J. A. Ott, K. B. Reuter, S. W. Bedell, and D. K. Sadana, "Principle of direct van der Waals epitaxy of single-crystalline films on epitaxial graphene," Nat. Commun. 5(1), 1–7 (2014).
- 94. H. S. Kum, H. Lee, S. Kim, S. Lindemann, W. Kong, K. Qiao, P. Chen, J. Irwin, J. H. Lee, S. Xie, S. Subramanian, J. Shim, S. H. Bae, C. Choi, L. Ranno, S. Seo, S. Lee, J. Bauer, H. Li, K. Lee, J. A. Robinson, C. A. Ross, D. G. Schlom, M. S. Rzchowski, C. B. Eom, and J. Kim, "Heterogeneous integration of single-crystalline complex-oxide membranes," Nature 578(7793), 75–81 (2020).
- 95. AH Heuer, RM Cannon, and NJ Tighe, Plastic Deformation in Fine-Grain Ceramics (Springer, 1968), pp. 339–365.
- W. R. Cannon and T. G. Langdon, Creep of Ceramics Part 2 An Examination of Flow Mechanisms, No. 1 (Kluwer Academic Publishers, 1988), 23.
- 97. F. R. N. Nabarro, Report of a Conference on Strength of Solids (The Physical Society, 1948).
- 98. C. Herring, "Diffusional viscosity of a polycrystalline solid," J. Appl. Phys. 21(5), 437–445 (1950).